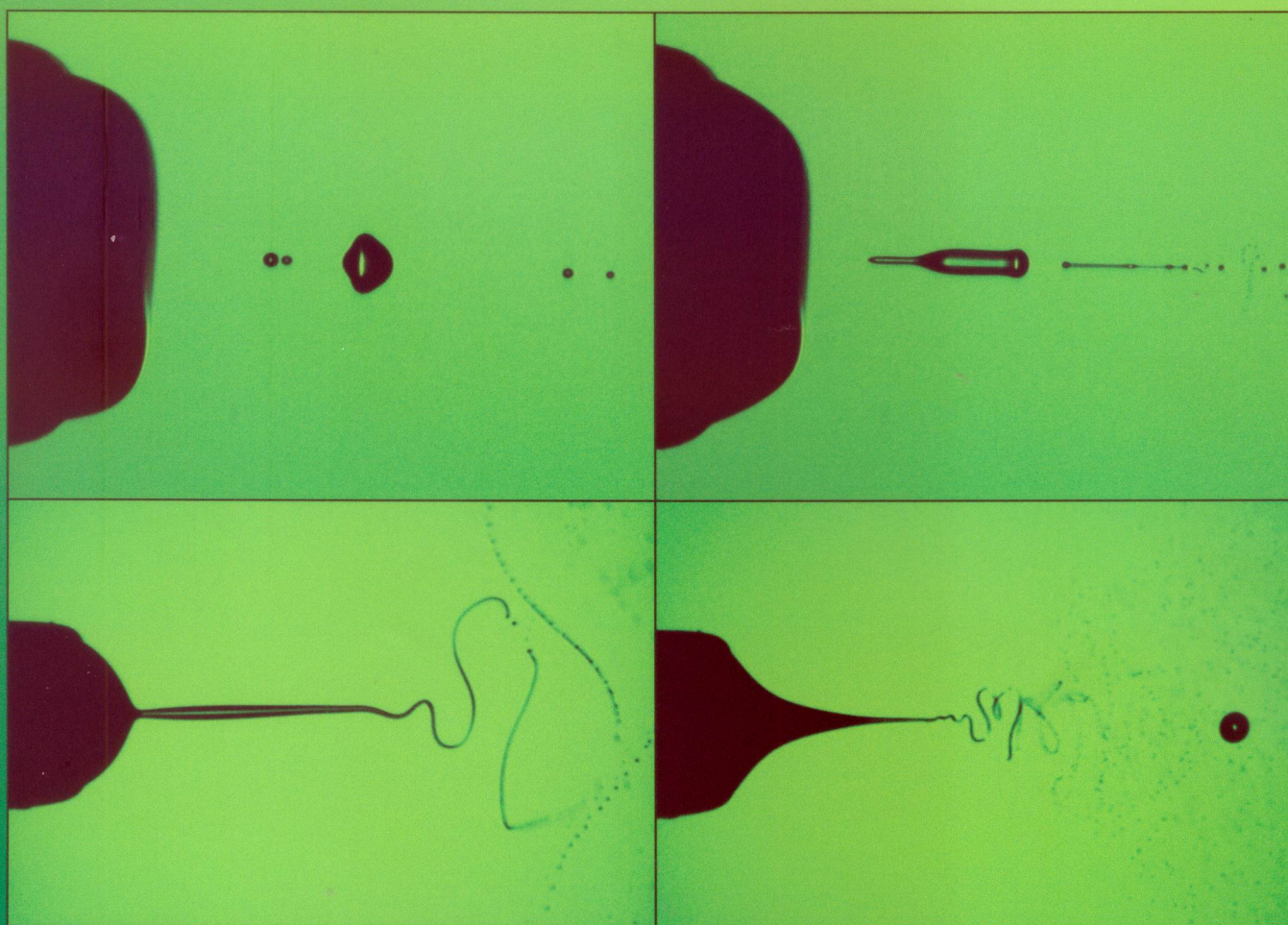


analytical chemistry

April 15, 2007

3105

Spraying Mode Effect on Droplet Formation and Ion Chemistry in Electrosprays



3041

Online Concentration and Affinity Separation of Biomolecules Using Multifunctional Particles in CE under Magnetic Field

3091

Comprehensive 2D FFF/LC in the Analysis of Large Molecules

Spraying Mode Effect on Droplet Formation and Ion Chemistry in Electrosprays

Peter Nemes, Ioan Marginean,[†] and Akos Vertes*

Department of Chemistry and W.W. Keck Institute for Proteomics Technology and Applications, George Washington University, Washington, D.C. 20052

Depending on the spraying conditions and fluid properties, a variety of electrospray regimes exists. Here we explore the changes in ion production that accompany the transitions among the three axial spraying modes, the burst mode, the pulsating Taylor cone mode, and the cone-jet mode. Spray current oscillation and phase Doppler anemometry measurements, fast imaging of the electrified meniscus, and mass spectrometry are utilized to study the formation, size, velocity, and chemical composition of droplets produced in the three modes. High-speed images indicate that the primary droplets are produced by varicose waves and lateral kink instabilities on the liquid jet emerging from the Taylor cone, whereas secondary droplets are formed by fission. Dramatic changes in the droplet size distributions result from the various production and breakup mechanisms observed at different emitter voltages and liquid flow rates. We demonstrate that droplet fission can be facilitated by space charge effects along the liquid jet and in the plume. Compared to the other two regimes, a significantly enhanced signal-to-noise ratio, a lower degree of analyte oxidation, and milder fragmentation are observed for the cone-jet mode.

Electrospray ionization (ESI) has enabled the transfer of macromolecules¹ and even viruses² into the gas phase as intact ions and opened new avenues in biochemical analysis. It aided the study of biologically relevant noncovalent interactions by mass spectrometry (MS),^{3–5} and a growing number of investigations utilized ESI-MS to follow changes in the tertiary structure of proteins.⁶

Although for biomedical applications ESI has become the ionization method of choice for routine mass spectrometric

analysis,^{7,8} relatively little is known about its mechanistic details. To further improve the ionization efficiency and the stability of this ion source, a fundamental understanding of the electrospray processes is required. The hydrodynamics of the electrified liquid meniscus,^{9–12} the ejection of charged liquid filaments and their breakup into droplets^{13,14} followed by droplet fission,^{15–17} and the eventual release of gas-phase ions^{18,19} are interconnected steps that have been studied separately. To better appreciate the relationship between the mechanism of spray formation and ion production, simultaneous spray characterization and ion yield measurements are needed.

A related question yet to be answered is the relationship between the structure and chemical composition of solution-phase analytes and the corresponding gas-phase ions. Whereas several studies suggest that the solution-phase information is (at least to some extent) preserved in the gas phase,^{3,4,20} this is not necessarily valid in all cases. Electrochemical reactions inherent to the nature of electrosprays²¹ have been shown to alter the composition and/or the pH of the solution,^{22–25} resulting in, for example, changes in the charge-state distributions of proteins.²⁶ Further processes arise from the acidification²⁷ and solvent fractionation of the evaporating droplets²⁸ moving downstream. For very large analytes

- (7) Rachel, L.; Winston, M. C. F. *Mass Spectrom. Rev.* **1997**, *16*, 165–179.
- (8) Domon, B.; Aebersold, R. *Science* **2006**, *312*, 212–217.
- (9) Hayati, I.; Bailey, A. I.; Tadros, T. F. *Nature* **1986**, *319*, 41–43.
- (10) Hayati, I.; Bailey, A.; Tadros, T. F. *J. Colloid Interface Sci.* **1987**, *117*, 222–230.
- (11) Hayati, I.; Bailey, A. I.; Tadros, T. F. *J. Colloid Interface Sci.* **1987**, *117*, 205–221.
- (12) Cloupeau, M.; Prunet-Foch, B. *J. Electrostat.* **1989**, *22*, 135–159.
- (13) Rayleigh, L. *Proc. London Math. Soc.* **1878**, *9*, 4–13.
- (14) Mutoh, M.; Kaieda, S.; Kamimura, K. *J. Appl. Phys.* **1979**, *50*, 3174–3179.
- (15) Taylor, G. I. *Proc. R. Soc. London, A* **1964**, *280*, 383–397.
- (16) Rayleigh, L. *Philos. Mag.* **1882**, *14*, 184–186.
- (17) Gomez, A.; Tang, K. *Phys. Fluids* **1994**, *6*, 404–414.
- (18) Dole, M.; Mack, L. K.; Hines, R. L.; Mobley, R. C.; Ferguson, L. D.; Alice, M. B. *J. Chem. Phys.* **1968**, *49*, 2240–2249.
- (19) Iribarne, J. V.; Thomson, B. A. *J. Chem. Phys.* **1976**, *64*, 2287–2294.
- (20) Loo, J. A. *Mass Spectrom. Rev.* **1997**, *16*, 1–23.
- (21) de la Mora, J. F.; van Berkel, G. J.; Enke, C. G.; Cole, R. B.; Martinez-Sanchez, M.; Fenn, J. B. *J. Mass Spectrom.* **2000**, *35*, 939–952.
- (22) Blades, A. T.; Ikononou, M. G.; Kebarle, P. *Anal. Chem.* **1991**, *63*, 2109–2114.
- (23) van Berkel, G. J.; McLuckey, S. A.; Glish, G. L. *Anal. Chem.* **1992**, *64*, 1586–1593.
- (24) van Berkel, G. J.; Zhou, F. M.; Aronson, J. T. *Int. J. Mass Spectrom. Ion Processes* **1997**, *162*, 55–67.
- (25) Ochran, R. A.; Konermann, L. *J. Am. Chem. Soc.* **2004**, *126*, 1748–1754.
- (26) Konermann, L.; Silva, E. A.; Sogbein, O. F. *Anal. Chem.* **2001**, *73*, 4836–4844.
- (27) Zhou, S.; Prebyl, B. S.; Cook, K. D. *Anal. Chem.* **2002**, *74*, 4885–4888.

* To whom correspondence should be addressed. Phone: (202) 994-2717. Fax: (202) 994-5873. E-mail: vertes@gwu.edu.

[†] Present address: Environmental Molecular Sciences Laboratory, Pacific Northwest National Laboratory, P.O. Box 999, Richland, WA 99352.

- (1) Fenn, J. B.; Mann, M.; Meng, C. K.; Wong, S. F.; Whitehouse, C. M. *Science* **1989**, *246*, 64–71.
- (2) Fuerstenau, S. D.; Benner, W. H.; Thomas, J. J.; Brugidou, C.; Bothner, B.; Siuzdak, G. *Angew. Chem., Int. Ed.* **2001**, *40*, 541–544.
- (3) Ganem, B.; Li, Y.-T.; Henion, J. D. *J. Am. Chem. Soc.* **1991**, *113*, 6294–6296.
- (4) Katta, V.; Chait, B. T. *J. Am. Chem. Soc.* **1991**, *113*, 8534–8535.
- (5) Baca, M.; Kent, S. B. H. *J. Am. Chem. Soc.* **1992**, *114*, 3992–3993.
- (6) Chowdhury, S. K.; Katta, V.; Chait, B. T. *J. Am. Chem. Soc.* **1990**, *112*, 9012–9013.

there can be an interference between their size and that of the electrospray droplet; e.g., submicrometer droplets are found to constrain viral complexes and cause their fragmentation in the droplet formation or fission process.²⁹ This effect becomes increasingly important in nanosprays that generate 100–1000 times smaller droplets than regular electrosprays.³⁰

Electrostatic spraying is known to exhibit a variety of spraying modes. Classifications of these regimes have been suggested based on the morphology and dynamics of the liquid meniscus³¹ and on the time dependence of the spray current.³² A direct link has recently been established between the electrohydrodynamic pulsation of the liquid meniscus and the measured current oscillations,³³ providing a connection between the two taxonomies. Due to the lack of a consensus for the nomenclature of spraying modes, in the present work the following terms, suggested in other studies,^{32,34,35} are used interchangeably: burst or axial I mode, pulsating Taylor cone or axial II regime, and stable Taylor cone (cone-jet) or axial III mode. These regimes involve different spray formation mechanisms and yield varying droplet sizes.³⁴

As the ionization efficiency varies with the droplet size,³⁶ the analytical performance of ESI is likely to be affected in cases where electrospray mode changes occur due to the changing properties of the solution, such as in combinations with gradient elution in high-performance liquid chromatography (HPLC) and ultraperformance liquid chromatography (UPLC). Indeed, experiments have shown profound changes in the spray dynamics and in droplet size distributions upon varying the conductivity of the electrosprayed solution.³⁷ To mitigate these effects, an image analysis system was developed to automatically control the spraying mode of the system by adjusting the high voltage applied on the needle during gradient elution.³⁸

Changes between the spraying modes can also be introduced by altering the voltage on the capillary or the liquid flow rate. We have reported on a fundamental analogy between the droplet formation dynamics of electrosprays and a dripping faucet.³⁵ The applied potential in electrosprays results in order–chaos–order transitions between the burst and the pulsating Taylor cone modes. The charge on the Taylor cone and consequently on the produced droplets also influences the ion yield of the analyte. The amount of charge on the Taylor cone can be estimated with good precision from its pulsation frequency.³⁹ For capillaries with smaller internal diameters the emitted charge becomes increasingly significant. This partially explains why higher charge states are observed at reduced orifice diameters in nanosprays.^{40,41}

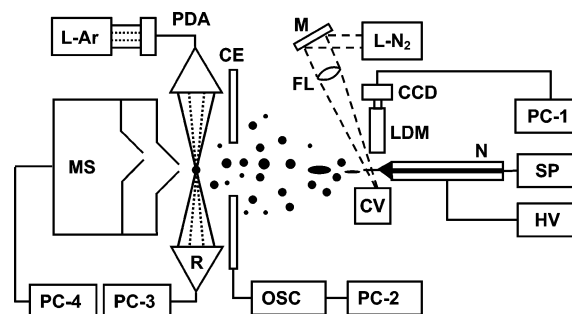


Figure 1. Schematics of the experimental setup: needle (N), syringe pump (SP), high-voltage power supply (HV), nitrogen laser (L-N₂), mirror (M), focusing lens (FL), cuvette (CV), CCD camera (CCD) with long-distance microscope (LDM) and personal computer (PC-1), counter electrode (CE), digital oscilloscope (OSC) with personal computer (PC-2), phase Doppler anemometer (PDA), argon ion laser source (L-Ar), receiver (R) with personal computer (PC-3), and mass spectrometer (MS) with personal computer (PC-4).

In this study we explore how changes in the electrospray regimes affect spray dynamics (such as the formation mechanism, size, and velocity of droplets) and ion generation. To address these processes, a combination of spray current measurements, fast imaging, phase Doppler anemometry, and mass spectrometry is utilized. First we report on the effect of the needle voltage and flow rate on the spray dynamics. Stroboscopic shadowgraphy is used to study the production of primary droplets from the ejected filaments and their fission into secondary droplets. This is followed by the comparison of the corresponding ionization efficiencies, the in-source fragmentation of the generated ions, and the extent of redox reactions in the various electrospray regimes.

EXPERIMENTAL SECTION

Figure 1 shows the schematics of the experimental setup. A home-built electrospray system with a low-noise syringe pump (Physio 22, Harvard Apparatus, Holliston, MA) was used to spray various solutions through stainless steel needles with a blunt tip, 260 μm i.d. and 510 μm o.d. (90525, Hamilton Co., Reno, NV), 130 μm i.d. and 260 μm o.d. (90531, Hamilton Co.), or with a tapered tip, 100 μm i.d. and 320 μm o.d. (New Objective, Woburn, MA). A stable high voltage was generated by a regulated power supply (PS350, Stanford Research Systems, Inc., Sunnyvale, CA) and was directly applied to the needle. A flat polished stainless steel plate counter electrode (38.1 mm \times 38.1 mm \times 0.6 mm) with a 6.0 mm diameter orifice in the center was placed perpendicular to the axis of the needle at a distance of 10 mm from the tip. The axis of the emitter was positioned in line with the center of the orifice by using an x – y – z mechanical translation stage (F38182 and NT37-979, Edmund Industrial Optics, Barrington, NJ). The probe volume of a two-color phase Doppler anemometer (PDA; Aerometrics Inc., Sunnyvale, CA) was located behind the counter electrode (on-axis, 13 mm away from the tip of the needle) to determine the size and velocity distributions of the electrosprayed droplets. The nature and yield of the produced gas-phase ions were determined by a mass spectrometer (JMS-T100LC AccuTOF mass spectrometer, JEOL Ltd., Peabody, MA).

(28) Zhou, S. L.; Cook, K. D. *Anal. Chem.* **2000**, *72*, 963–969.

(29) Hogan, C. J.; Kettleson, E. M.; Ramaswami, B.; Chen, D.-R.; Biswas, P. *Anal. Chem.* **2006**, *78*, 844–852.

(30) Wilm, M.; Mann, M. *Anal. Chem.* **1996**, *68*, 1–8.

(31) Cloupeau, M.; Prunet-Foch, B. *J. Aerosol Sci.* **1994**, *25*, 1021–1036.

(32) Juraschek, R.; Röllgen, F. W. *Int. J. Mass Spectrom.* **1998**, *177*, 1–15.

(33) Marginean, I.; Parvin, L.; Heffernan, L.; Vertes, A. *Anal. Chem.* **2004**, *4202*–4207.

(34) Cloupeau, M.; Prunet-Foch, B. *J. Electrostat.* **1990**, *25*, 165–184.

(35) Marginean, I.; Nemes, P.; Vertes, A. *Phys. Rev. Lett.* **2006**, *97*, 064502.

(36) Bruins, A. P.; Covey, T. R.; Henion, J. D. *Anal. Chem.* **1987**, *59*, 2642–2646.

(37) Olumee, Z.; Callahan, J. H.; Vertes, A. *J. Phys. Chem. A* **1998**, *102*, 9154–9160.

(38) Valaskovic, G. A.; Murphy, I. J. P.; Lee, M. S. *J. Am. Soc. Mass Spectrom.* **2004**, *15*, 1201–1215.

(39) Marginean, I.; Nemes, P.; Parvin, L.; Vertes, A. *Appl. Phys. Lett.* **2006**, *89*, 064104.

(40) Li, Y.; Cole, R. B. *Anal. Chem.* **2003**, *75*, 5739–5746.

(41) Ek, P.; Sjødahl, J.; Roeraade, J. *Rapid Commun. Mass Spectrom.* **2006**, *20*, 3176–3182.

The orifice of the sampling cone was lined up on-axis with the electrospray emitter at a distance of 15 mm from its tip. Thus, the probe volume of the PDA ($\sim 200 \mu\text{m}$ in width) was positioned ~ 2 mm from the sampling orifice. This allowed us to sample the same part of the spray plume with both the PDA and the mass spectrometer. Special care was taken to shield the spray assembly with a Faraday cage and a plastic enclosure to minimize the interference of electromagnetic fields and air currents, respectively.

Spray Current Measurements. The spray current was measured on the counter electrode described above by a 500 MHz digital oscilloscope (WaveSurfer 452, LeCroy, Chestnut Ridge, NY). Each spray current measurement consisted of 250 000 data points collected at a 25 kHz sampling rate. The data were processed with the embedded software of the oscilloscope. Special care was taken to allow the electrospray system to stabilize every time after adjustment of the spray conditions (e.g., high voltage or flow rate).

Fast Taylor Cone Imaging. The Taylor cone pulsation and the filament breakup were imaged by a fast camera (QICAM, QImaging, Burnaby, BC, Canada) equipped with a long-distance microscope (KC, Infinity Photo-Optical Co., Boulder, CO), and the cone was back-illuminated with a flash source. The illumination was achieved by utilizing the fluorescent emission from a laser dye solution (coumarin 540A, Exciton, Dayton, OH) upon excitation with a 337.1 nm nitrogen laser (VSL-337, Newport Corp., Irvine, CA). The dye was dissolved in ethanol (reagent grade, Sigma-Aldrich) at a concentration of 3×10^{-5} M, and the solution was stored in a sealed quartz cuvette. Spectrofluorometric measurements (RF-5301PC, Shimadzu Corp., Kyoto, Japan) on the solution at an excitation wavelength of 337 nm showed intense fluorescence with a maximum at 512 nm. Thus, the fluorescence of the solution could be used as a green flash light source. Using a fast photodiode (Det2-Si, Thorlabs Inc., North Newton, NJ) and a 1.5 GHz digital oscilloscope (LC684DXL, LeCroy), the laser pulse and lifetime of the fluorescent illumination were measured to be 3.4 ± 0.1 and 7.3 ± 0.3 ns at fwhm, respectively.

For efficient illumination of the Taylor cone, the dye solution was excited at a $\sim 45^\circ$ angle with respect to the axis of the camera in the plane of the long-distance microscope (see Figure 1). The images presented in this paper were taken with a 40 μs exposure time using the acquisition software of the camera (Qcapture, version 2.58, Quantitative Imagine Corp.). The 7 ns flash illumination enabled us to overcome the exposure time limitation of the camera and to study the fast dynamics of the meniscus in exquisite detail (see the three movies in the Supporting Information). Temporal changes in the spray current were used to trigger a delay generator (DG535, Stanford Research Systems). This device provided variable-delay triggers for the camera and the nitrogen laser. The images were processed with Adobe Photoshop, version 7.0 (Adobe, San Jose, CA).

Phase Doppler Anemometry. Due to the geometric conflict of the mass spectrometer and the PDA system, the latter had to be suspended in an inverted position. The performance of the PDA system was optimized as reported elsewhere.^{37,42} For each measurement 10 000 data points were collected and analyzed with the DataView software (version 1.1, Aerometrics Inc.). Droplet size distributions with more than one maximum were deconvoluted, and the mean droplet sizes, velocities, and corresponding

distribution widths were extracted from the Gaussian fit parameters with a scientific visualization package (Origin 6.0, OriginLab Co., Northampton, MA).

Mass Spectrometry. The commercial ion source of the mass spectrometer was removed, and the home-built electrospray source, described above, was aligned on the axis of the sampler cone. The ion-transfer optics of the mass spectrometer was optimized for optimum signal intensity and resolution. Mass analysis was performed in positive ion mode in an m/z range of 10–1000. Each mass spectrum was acquired as the average of 90 spectra at a 1 s/spectrum integration rate. Data acquisition and processing was performed with the MassCenter software (version 1.3.0, JEOL Ltd.). Control experiments confirmed that the irradiation of the droplets by the blue (488 nm) and green (515 nm) argon ion laser beams used in the PDA or the illumination for the fast imaging setup at wavelengths 337 and 512 nm did not affect the production of ions. This enabled simultaneous analysis by the PDA and the mass spectrometer.

Chemicals. Ultrapure water (18.3 M Ω cm) was produced using a deionization system (E-pure D4631, Barnstead, Dubuque, IA). HPLC-grade methanol (Sigma-Aldrich) was used to prepare the 50% (v/v) aqueous solvent mixture for the 1×10^{-5} M solutions of reserpine (reagent grade, Sigma-Aldrich), leucine enkephalin (reagent grade, Sigma-Aldrich), and 3-methoxybenzylpyridinium chloride (3MO-BP; reagent grade, Celestial Specialty Chemicals, Nepean, ON, Canada). Unless otherwise noted these solutions were acidified with glacial acetic acid (TraceSelect grade, Sigma-Aldrich) at 0.1% (v/v) concentration. The electrical conductivity of the solutions was measured with a conductivity meter equipped with a dip cell (YSI 3100, YSI Inc., Yellow Springs, OH). The pH values of the solutions were determined using a combined glass electrode (S90528, Fischer Scientific). The conductivities of the electrosprayed solutions were $3.5 \pm 0.2 \mu\text{S}/\text{cm}$ for the 50% (v/v) methanol solution and $36.1 \pm 0.2 \mu\text{S}/\text{cm}$ for the same containing 0.1% (v/v) acetic acid. The corresponding pH values were 5.96 ± 0.07 and 3.80 ± 0.06 , respectively.

RESULTS AND DISCUSSION

Spraying Modes and Droplet Characteristics. Operating parameters (e.g., needle voltage and liquid flow rate) are of major importance in defining the spraying modes in electrosprays. These modes are determined by the electrohydrodynamic disintegration mechanism of the liquid meniscus and result in profoundly different droplet characteristics, such as size and velocity distributions, in the spray plume. The diversity of the meniscus dynamics is most apparent from the movies in the Supporting Information based on fast imaging. Axial spraying modes can also be distinguished by monitoring the spray current on the counter electrode (see typical examples for a 50% methanol solution in Figure 2). On the basis of the current patterns, the naming of these regimes is self-explanatory. In Figure 2, the burst (or axial I) mode in green shows occasional rise and oscillation of the current followed by a period of inactivity.³⁵ In the pulsating Taylor cone (or axial II) mode, the current oscillations are regular with a well-defined period (black curve in Figure 2). Finally the cone-jet (or axial III) mode exhibits a higher dc current component than the other two modes with no or minimal ac contribution (red curve in Figure 2). Sudden changes in the current (e.g., a rising edge in a current

(42) Olumee, Z.; Callahan, J. H.; Vertes, A. *Anal. Chem.* **1999**, *71*, 4111–4113.

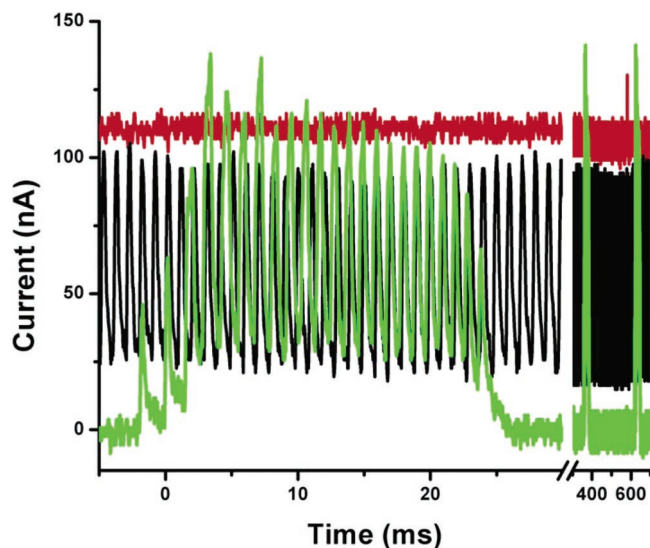


Figure 2. Spray current measurement for 3MO-BP solution in spraying regimes axial I (green), II (black), and III (red) at emitter (Hamilton 90525) potentials 2750, 2950, and 4050 V, respectively. The flow rate was 1 $\mu\text{L}/\text{min}$.

oscillation) were used to trigger the imaging system shown in Figure 1.

Fast imaging of the meniscus region enabled us to reproducibly follow the production and initial fission of primary droplets in the different spraying modes. Figure 3 compares the typical meniscus shapes and their disintegration for 50% methanol solution in the three axial spraying modes. The top three panels show the different phases of liquid ejection in a single current spike of the burst mode (axial I). Initially the liquid filament exhibits kink instabilities and produces relatively small droplets. The majority of the ejected liquid, however, is carried away by a few very large droplets that vary in initial shape between a spindle and a bottle (see the detailed evolution of the process in the axial I movie in the Supporting Information). These shapes relax into oscillating large droplets that occasionally undergo division. This process is driven by the fluid dynamics of the oscillation and results in approximately equally sized offspring (see the large droplet in the top right panel). Such equal division is in sharp contrast to the fission of droplets with close to critical charge, which exhibit the ejection of much smaller droplets. Compared to the smaller droplets emitted initially, these large droplets carry a smaller amount of charge per volume and require additional generations of fission to become sufficiently small for ion production. Thus, they do not contribute significantly to the ion signal.

The middle panel is an example of liquid ejection in pulsating Taylor cone mode (axial II). A spindle-like large droplet is accompanied by a significant amount of smaller ones produced by the lateral kink instabilities at the end of the jet (see the two axial II movies in the Supporting Information). As these pulsations repeat themselves periodically, compared to the axial mode I both the larger quantity of small droplets and the higher duty cycle contribute to the increased ion production in this mode. The steady cone-jet (axial III) mode is presented in the bottom panel. This mode is stationary with no major changes in the shape of the meniscus. It produces much smaller droplets that downstream become undetectable by the PDA. As is later demonstrated, the ion production is most efficient in this mode.

In all three modes, the production of small analytically useful droplets was observed at the end of the filament. The two main filament disintegration mechanisms were the formation and pinching of varicose instabilities and the whipping motion of the kink instabilities.⁴³ Images in Figure 3B,C show close-ups of the varicose waves on the surface of the jet. As these waves propagate along the charged filament, primary droplets (P) of differing sizes are pinched off. The largest droplets (P_1) are initially connected by liquid bridges. These bridges later separate and form the smaller droplets (P_2 and P_3 through a similar but asymmetric process) that are on-axis with the large ones. These two types of droplets are directly formed from the filament breakup and thus can both be considered primary droplets. Secondary droplets (S) are formed downstream by fission due to the space charge effects induced by the field of neighboring primary droplets and as a result of solvent evaporation from the primary droplets.

For example, in the cone-jet spraying mode the primary droplet size is determined by the diameter of the filament and the wavelength of the varicose waves before breakup.^{12,13} Additional factors include the flow rate,¹² the electrical conductivity, and the viscosity⁴⁴ of the fluid along with the charge transported by the filament.^{14,45}

Burst Mode. Methanol solutions (50%, v/v) were electrospayed at a 5.0 $\mu\text{L}/\text{min}$ flow rate. At the onset potential of the spray (2500 V), axial mode I ensued and a trimodal droplet size distribution was observed by the PDA. Deconvolution of this distribution into three Gaussians (see, for example, Figure 4A, left panel) showed the components to be centered at 10.4 ± 2.2 , 17.9 ± 1.8 , and $35.7 \pm 1.2 \mu\text{m}$ with distribution widths of 5.1, 4.2, and 2.8 μm , respectively. Generation of the droplets of corresponding sizes in close proximity to the spraying tip was confirmed by imaging experiments (see later).

Because in this regime a substantial portion of the liquid is carried by large droplets, additional generations of fission have to take place to disperse the liquid and reach the size range of $\sim 10 \text{ nm}$ and below most efficient for ion production.¹⁹ As is shown later, this results in marginal ion production. Therefore, in analytical applications the initial optimization of ion source performance is likely to steer the spray away from axial mode I operating conditions. It is, however, possible that in experiments with changing liquid composition (e.g., gradient elution) axial mode I conditions result.

Applying higher voltages on the needle or increasing the liquid flow rate induced significant changes in the spray dynamics. For example, as the emitter potential was increased from 2500 to 2800 V the modality of the droplet size distributions changed from trimodal to bimodal (see Figure 4). For a wider range of voltages, Figure 5 shows the mean values of the deconvoluted distributions. As the voltage was increased and the spray transitioned from burst mode to pulsating Taylor cone mode, a merging of the underlying size distributions was observed. The initial trimodal distribution first (at 2800 V) turned bimodal, which at 2950 V, at the onset of axial mode II, became monodisperse. Similar effects were observed as the flow rate was raised from 5.0 to 18.0 $\mu\text{L}/\text{min}$ at a constant emitter potential (at 2800 V, data not shown). Spray

(43) Hartman, R. P. A.; Brunner, D. J.; Camelot, D. M. A.; Marijnissen, J. C. M.; Scarlett, B. *J. Aerosol Sci.* **2000**, *31*, 65–95.

(44) Weber, C. Z. *Angew. Math. Mech.* **1931**, *11*, 136–154.

(45) Bailey, A. G.; Balachandran, W. *J. Electrostat.* **1981**, *10*, 99–105.

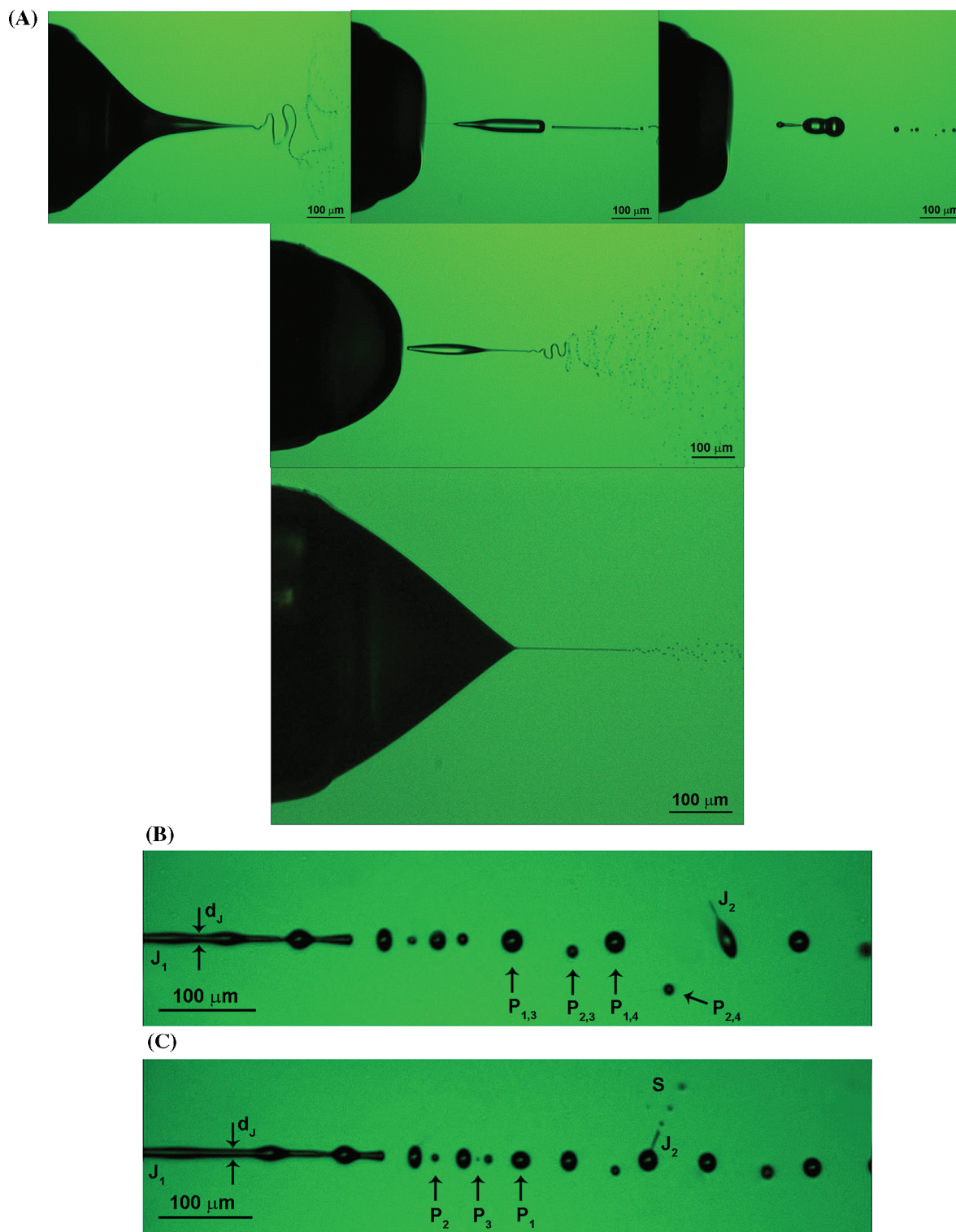


Figure 3. (A) Comparison of typical meniscus shapes and disintegration in three axial spraying modes. The top three panels show the different phases of liquid ejection in a single current spike of the burst mode (axial I). Initially the liquid filament exhibits kink instabilities and produces relatively small droplets. The majority of the ejected liquid is carried away by a few very large droplets that vary in initial shape between a spindle and a bottle. These large droplets require additional generations of fission to become sufficiently small for ion production; thus, they do not contribute significantly to the ion signal. The middle panel is an example of liquid ejection in pulsating Taylor cone mode (axial II). A spindle-like large droplet is accompanied by a significant amount of smaller ones produced by lateral kink instabilities at the end of the jet. The steady cone-jet (axial III) mode is presented in the bottom panel. This mode is stationary with no major changes in the shape of the meniscus. It produces much smaller droplets that downstream become undetectable by the PDA. Ion production is most efficient in this mode. (B) and (C) show the filament breakup in axial mode I (Hamilton 90525 needle at 2800 V) through varicose instabilities. Fission of primary droplets can be observed through secondary jets in the radial direction.

current measurements indicated that changes in the modality of the size distributions in the axial I to II transition region were

accompanied by bistable spraying that was alternating in time between axial modes I and II.

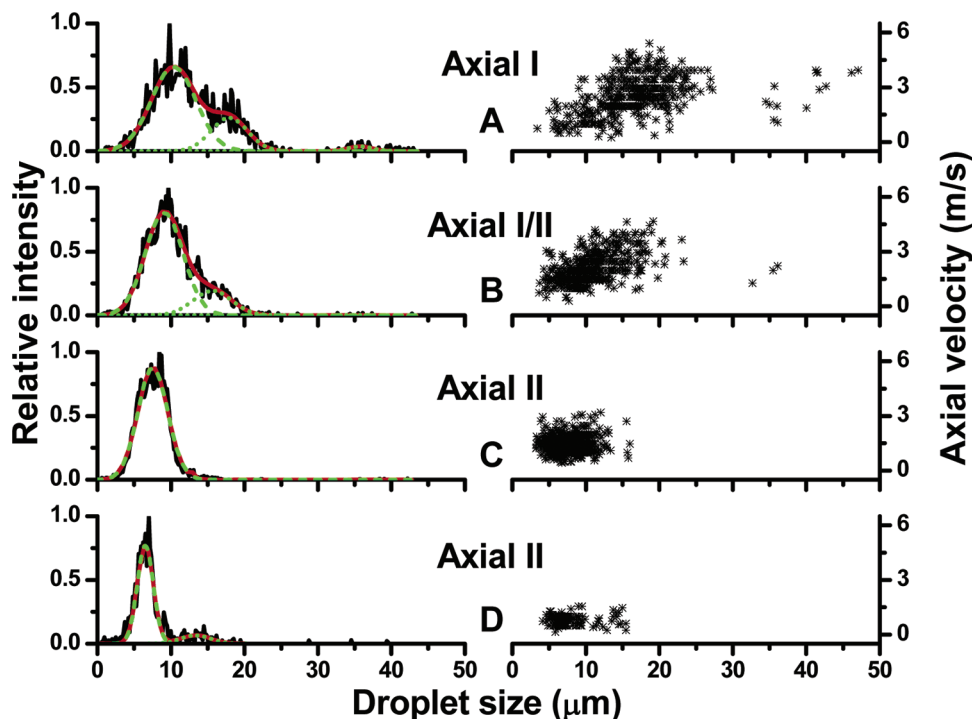


Figure 4. Droplet diameter distributions (black lines in left panels) and corresponding diameter–velocity correlations (right panels) for 50% methanol solutions electrospayed at a constant $5.0 \mu\text{L}/\text{min}$ flow rate and emitter voltages of (A) 2500, (B) 2800, (C) 3100, and (D) 3400 V. Deconvoluted Gaussian peaks in the left panels are shown by dashed and dotted green lines, whereas the combined curves are in solid red.

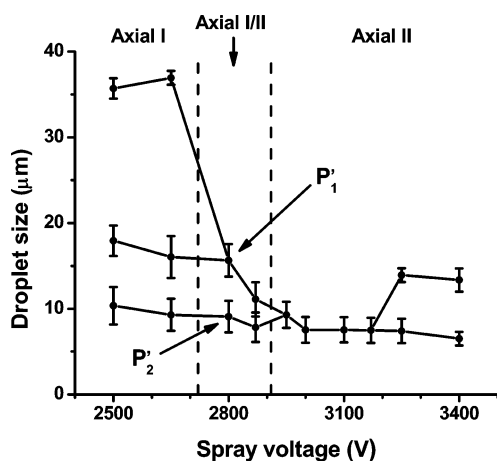


Figure 5. Modalities of droplet size distributions for 50% methanol as a function of spraying voltage at a $5.0 \mu\text{L}/\text{min}$ flow rate. Vertical dashed lines indicate transitions between axial regimes established.

Analysis of our imaging results for a 2800 V spray voltage (see, for example, Figure 3B) indicates that, in this transition regime between axial modes I and II, the diameters of the jet, d_j , and the large primary droplets (P_1), d_D , are 10.7 ± 0.9 and $18.6 \pm 1.2 \mu\text{m}$, respectively. Figure 3C shows similar results for the mean diameters, 11.7 ± 0.3 and $21.2 \pm 1.7 \mu\text{m}$. The corresponding d_D/d_j ratios, 1.74 ± 0.18 and 1.81 ± 0.15 , respectively, are slightly lower than the previous theoretical^{13,46} and experimental^{12,14,45,47} results of $d_D/d_j = 1.89$ for stable cone jets. As is apparent from Figures 4 and 5, these droplets shrink to a diameter of $15.6 \pm 1.9 \mu\text{m}$ after traveling ~ 11 mm downstream from the point of their formation. The most abundant component of the size distribution

measured by the PDA shows a mean value of $9.1 \pm 1.8 \mu\text{m}$, in good correlation with the sizes of the smaller primary droplets, P_2 ($10.2 \pm 0.9 \mu\text{m}$ from imaging), produced by the relaxation of the liquid bridges between the larger ones.

The image in Figure 3B shows that the disintegration of the jet, J_1 , yields more of the larger primary droplets (e.g., $P_{1,3}$ and $P_{1,4}$), yet the most abundant component of the droplet size distribution (see the first peak in the 2800 V panel of Figure 4) is similar in size to the smaller primary droplets (e.g., $P_{2,3}$ and $P_{2,4}$). This indicates that the larger primary droplets shrink in size between the end of the filament and the PDA probe volume. The two most important processes responsible for this size reduction are Coulomb fission and solvent evaporation.

Indeed, the images in Figure 3B,C show large primary droplets undergoing a fission event shortly after the detachment from the liquid jet, J_1 . Unlike other images of charged droplet fission captured in the spray plume,¹⁷ our pictures demonstrate that secondary liquid jets, J_2 , can form shortly after detachment, while the droplet is still on-axis. Moreover, in Figure 3C three offspring droplets of similar size ($d_{SD} = 3.0 \pm 0.6 \mu\text{m}$) are being ejected through a side filament apparently still attached to the parent droplet ($d_D = 20.5 \pm 0.8 \mu\text{m}$). This rupture translates into a loss of 0.9% in mass, showing a reasonable agreement with the 1–5% obtained for levitated microdroplets.^{48–50} In Figure 3B, a droplet distorted in shape is captured at the moment of jet ejection. The anticipated evolution from this stage is similar to what is seen in Figure 3C, i.e., the breakup of the J_2 filament into secondary droplets while the parent droplet itself regains its spherical shape.

(48) Smith, J. N.; Flagan, R. C.; Beauchamp, J. L. *J. Phys. Chem. A* **2002**, *106*, 9957–9967.

(49) Grimm, R. L.; Beauchamp, J. L. *Anal. Chem.* **2002**, *74*, 6291–6297.

(50) Li, K. Y.; Tu, H. H.; Ray, A. K. *Langmuir* **2005**, *21*, 3786–3794.

(46) Tyler, E. *Philos. Mag.* **1933**, *16*, 504–518.

(47) Jones, A. R.; Thong, K. C. *J. Phys. D: Appl. Phys.* **1971**, *4*, 1159–1166.

In our imaging experiments, ejection of the secondary jet, J_2 , and offspring droplets, S, occurred in the radial direction with respect to the primary jet, J_1 . Studying monodisperse spray generation for combustion, Gomez and Tang¹⁷ reported similar behavior for a fuel model, heptane doped with an antistatic fuel additive. They considered aerodynamic and space-charge effects caused by other charged droplets as a plausible explanation. They also pointed out that the unstable droplets do not undergo energetic disintegration (i.e., Coulomb explosion) as had been suggested by earlier studies.^{1,51} Our images serve as direct proof that this space charge-assisted disintegration mechanism prevails for water–methanol systems and, very likely, for other solutions commonly used in ESI.

Notably, the smaller droplets ($d < \sim 4 \mu\text{m}$) observed by imaging were not detected by the PDA system. A possible explanation is that, due to the droplet shrinking discussed above, by the time they reach the PDA probe volume, they shrink below the $\sim 1 \mu\text{m}$ cutoff for detection. In addition, space charge effects move the smaller droplets off-axis and thus out of the probe volume.¹⁷ This radial segregation started very close ($\sim 1 \text{ mm}$) to the tip of the emitter. For example, in Figure 3B two smaller primary droplets, $P_{2,3}$ and $P_{2,4}$, are located off-axis. In first approximation, there are three radial forces acting on the droplets: the Coulomb repulsion between the charged droplets, the aerodynamic drag force, and the gravitational force. Of these interactions, the gravitational force is significantly smaller than the other two; thus, its effect on the droplet movement can be neglected. Knowing the sizes ($\sim 11 \mu\text{m}$ from Figure 3B) and the approximate velocities ($\sim 2 \text{ m/s}$ from Figure 4) of the droplets from the imaging and the PDA measurements, respectively, one can easily verify whether these forces are responsible for their radial displacement. The $\sim 100 \mu\text{m}$ axial displacement of $P_{2,3}$ to the axial position of $P_{2,4}$ corresponds to a $50 \mu\text{s}$ flight time. Numerical integration of the radial equations of motion (with the Coulomb and Stokes force terms) for this time period indicates that the expected radial displacement of $P_{2,3}$ is $\sim 60 \mu\text{m}$. This is in good agreement with the measured $\sim 52 \mu\text{m}$ distance between the position of the $P_{2,4}$ droplet and the axis of the J_1 jet. This demonstrates that the radial dispersion of the smaller primary droplets can be explained by space charge effects.

Pulsating Taylor Cone Mode. As the emitter potential was further increased the spray current measurements indicated that the spraying mode stabilized in the pulsating Taylor cone mode. Simultaneously, the PDA measurements showed that the spray, at least locally, became monodisperse. For example, at 3100 V the mean and the width of the droplet diameter distribution were 7.5 ± 1.5 and $3.4 \mu\text{m}$, respectively (see Figure 4). The droplet size–axial velocity correlation data, shown on the right side of Figure 4, indicated that the change in the spraying regime was accompanied by a compression of both the size and the axial velocity distributions. The axial velocities ranged between ~ 0.5 and 3 m/s compared to the ~ 0.5 – 6 m/s spread seen at 2500 V (Figure 4).

The imaging experiments at 3100 V (not shown) indicated that the filament ($d_j = 5.0 \pm 0.3 \mu\text{m}$) broke up into approximately equally spaced droplets of $d_D = 8.6 \pm 1.5 \mu\text{m}$ diameter, yielding

a d_D/d_j ratio of 1.72 ± 0.32 . The axial trajectories of the droplets generated under these spraying conditions proved to be quite stable compared to those observed at 2800 V. Radial displacement for these droplets was noticed only after they had traveled $\sim 3 \text{ mm}$, whereas in the 2800 V case this was significantly shorter ($\sim 1 \text{ mm}$). The reduced radial dispersion at 3100 V compared to 2800 V on a given distance can be explained either by assuming that the produced droplets carry less charge, resulting in a diminished space charge effect, or by the higher axial velocity of the droplets at the elevated voltage.

Further increasing the emitter potential resulted in the reappearance of bimodal droplet size distributions. For example, at 3400 V in Figure 4 two components in the size distributions are detected. An example of this spraying mode for smaller emitter diameters (i.d. $130 \mu\text{m}$ and o.d. $260 \mu\text{m}$) established at lower (2000 V) potential was captured using time-lapse imaging triggered by the current oscillations. (See the related movie in the Supporting Information.) We noticed that the leading end of the jet emerging from the Taylor cone showed increased bending instability. Shortly after its detachment from the cone, the trailing end of the filament transformed into a spindle-like shape and the whipping of the leading end diminished. This seems to be an indication of excessive charge being present on and carried away by the filament experiencing kink-type instabilities.³⁴ The spindle then broke up into two parts. The leading end of the filament disintegrated into droplets $5 \pm 1 \mu\text{m}$ in diameter, whereas the trailing spindle-shaped volume relaxed into a droplet $31 \pm 2 \mu\text{m}$ in diameter. Thus, at higher voltages the filament ejected from a pulsating Taylor cone first expels fine droplets through a whipping motion. These finer droplets are radially dispersed and known to undergo several generations of fission and produce the majority of the ions (see below). The remaining liquid in the spindle relaxes into much larger droplets that are likely to yield a negligible amount of ions and do not contribute to the analytical signal.

Cone-Jet Mode. Further increasing the emitter potential produced the cone-jet or axial III spraying mode. In this mode the Taylor cone becomes stationary and the liquid jet diameter significantly decreases (see the bottom panel in Figure 3A). The imaging experiments revealed the shortening and thinning of the filament and the generation of droplets that were significantly smaller than those formed in burst or pulsating Taylor cone modes. The resulting fine ($< 3 \mu\text{m}$) droplets were radially dispersed by a slight kink instability of the jet. By the time the produced droplets reached the probe volume, their diameter dropped below the $\sim 1 \mu\text{m}$ cutoff of the PDA detection and did not yield a PDA signal. Formation of submicrometer droplets in electrostatic spraying had already been observed by using a differential mobility analyzer.⁵²

Ion Yields in Different Spraying Modes. To compare the efficiency of ion generation among various spraying modes, a $1 \times 10^{-6} \text{ M}$ solution of leucine enkephalin was prepared in 50% methanol and fed through a metal capillary at a $5.0 \mu\text{L}/\text{min}$ flow rate. The high voltage was adjusted to establish stable axial I, II, and III modes. We measured the size and the velocity of the droplets and simultaneously mass analyzed the ions produced.

First, axial mode I was maintained by applying 2700 V on the emitter. As shown in Figure 5 above, on the spray axis the size

(51) Wilm, M. S.; Mann, M. *Int. J. Mass Spectrom. Ion Processes* **1994**, *136*, 167–180.

(52) de Juan, L.; de la Mora, J. F. *J. Colloid Interface Sci.* **1997**, *186*, 280–293.

distributions exhibited three components. By sampling the spray off-axis, we found that the largest (35–40 μm) droplets were present only close to the centerline of the spray, whereas the skirt of the spray consisted of 17–20 and 8–10 μm diameter droplets. These results indicated a size-based segregation of the droplets in the radial direction consistent with earlier observations for different solvents (*n*-heptane solutions).⁵³ In this burst regime, sampling by the mass spectrometer showed no analyte ion production at any position in the spray. It appears that the charge-to-volume ratio of these droplets was too small to efficiently produce gas-phase ions in this spraying mode.

In the pulsating Taylor cone regime, however, the mass analysis showed that both protonated and sodiated leucine enkephalin ions were formed. Their total intensity after background subtraction was relatively low, only 197 ± 18 counts/s at 3950 V. No significant variance was observed in the composition or in the intensities of these ions as a function of the radial position. This might be related to the radial mixing due to the whiplash motion of the filament. Mainly smaller ($\sim 5 \mu\text{m}$) droplets were measured by the PDA, but the presence of larger droplets (15 μm) was also detected in small abundances (data not shown). Off-axis the droplet size distributions were also unchanged.

Remarkably higher analyte ion yields were measured in cone-jet mode (axial mode III), at a needle voltage of 4000 V. The measured total abundance of the analyte after background correction was 669 ± 75 counts/s, 3 times higher than that recorded for axial mode II. As the spraying mode changed from the pulsating Taylor cone mode to the cone-jet mode, the background noise also decreased by a factor of 2, further improving the signal-to-noise ratio. These results are consistent with those of Valaskovic et al., who found that the pulsating Taylor cone and stable cone-jet regimes gave better ion signals.³⁸ Our results also indicated that similarly to the pulsating Taylor cone mode, no significant change in the composition or in the intensities of the ions was noticed upon radially mapping the spray. These data demonstrated that improved analytical sensitivity was achievable by operating the electrospray in cone-jet mode.

Analyte Ion Fragmentation. We explored whether a change in spraying regimes, that is, between axial modes II and III, is accompanied by a difference in analyte ion dissociation. Aqueous methanol (50%) solutions of 1×10^{-5} M reserpine containing 0.1% (v/v) acetic acid were fed through the tapered tip (100 μm i.d.) metal emitter at a 1.0 $\mu\text{L}/\text{min}$ flow rate. Thermometer ions (3MO-BP) were added to these solutions at 1×10^{-5} M concentration. In two separate sets of experiments in-source collision-induced dissociation (CID) was performed on the thermometer ions and reserpine to produce molecular ions and fragment ions at comparable intensities. The CID conditions were carefully optimized to activate only the 3MO-BP fragmentation and leave the reserpine coanalyte undissociated (see Figure 6A).

Mass analysis of the produced ions revealed that the reserpine also underwent some chemical changes. It appeared as a (reserpine - 2H + H)⁺ species at considerable intensities and as a (reserpine - 4H + H)⁺ ion at substantially lower abundances (see the logarithmic intensity scale in the inset of Figure 6A). Control experiments showed that the formation of these oxidized analyte species was not influenced by varying the CID conditions.

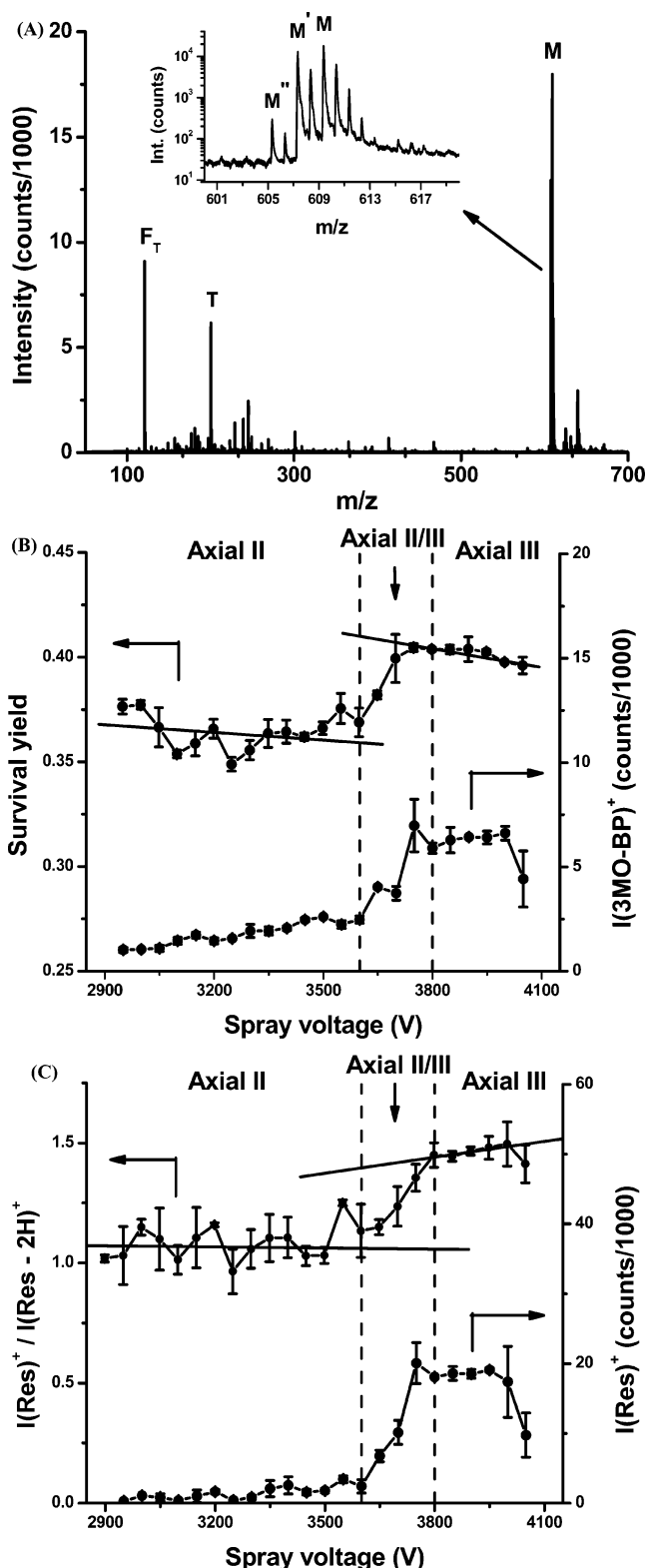


Figure 6. (A) Mass spectrum of a 50% methanol solution of 3MO-BP salt mixed with reserpine sprayed in cone-jet mode (3800 V). (B) Survival yields (left axis) and molecular ion intensities (right axis) of 3MO-BP. (C) Reduced-to-oxidized protonated molecular ion ratios (left axis) and molecular ion intensities (right axis) for reserpine. Vertical dashed lines indicate boundaries of the observed spraying modes. Equations for linear regression are $SY_{\text{axial III}} = 0.517 + (2.984 \times 10^{-5})U_{\text{spray}}$ and $SY_{\text{axial II}} = 0.403 + (1.232 \times 10^{-5})U_{\text{spray}}$ for 3MO-BP, $[(\text{Res})^+]/[(\text{Res} - 2\text{H})^+]_{\text{axial II}} = 1.115 - (1.485 \times 10^{-5})U_{\text{spray}}$, and $[(\text{Res})^+]/[(\text{Res} - 2\text{H})^+]_{\text{axial III}} = 0.596 + (2.222 \times 10^{-4})U_{\text{spray}}$, where U_{spray} is the spray voltage.

(53) Tang, K.; Gomez, A. *Phys. Fluids* **1994**, *6*, 2317–2332.

Increasing the liquid flow rate in the emitter, however, effectively suppressed their formation. These results allowed us to exclude the possibility of reserpine fragmentation through hydrogen loss and to perceive the process as the electrochemical oxidation of reserpine.

The survival yield method⁵⁴ was used to characterize the in-source CID of the thermometer ion, 3MO-BP, as a function of the spraying regime. Under the selected CID conditions the dissociation of the thermometer ion, T^+ , occurred in one channel only, $T^+ \rightarrow F_T^+ + N$, resulting in an ionized and a neutral fragment, respectively. The survival yield was calculated as $SY = I(T^+)/[I(T^+) + I(F_T^+)]$, where I represented the absolute intensity of a given ion. Remarkably, unlike in the case of leucine enkephalin before, the 3MO-BP ions were even recorded in the axial I spraying mode (at 2750 V), although only with a low signal intensity of 86 ± 5 counts/s. This difference can be attributed to the presence of preexisting ions in the 3MO-BP salt solution.

Compared to axial mode I, the ionization efficiency of the electrospray source was dramatically improved in axial regime II. The measured 3MO-BP ion abundances and the calculated thermometer ion survival yields as a function of emitter voltage are shown in Figure 6B. At the onset of the pulsating Taylor cone mode (2950 V) the signal intensity was 1025 ± 119 counts/s, more than 10 times higher than what was recorded in the burst mode. Increasing the emitter potential yielded a slowly increasing 3MO-BP ion yield. At 3600 V, the end of the axial II stability region, the signal intensity was 2470 ± 181 counts/s, which corresponded to a ~ 2.4 times improvement in the ionization efficiency within the axial II mode. Fourier analysis of the spray current showed that, compared to axial mode I, in axial mode II the improved ion yield could be explained by the ~ 15 -fold increase in the duty cycle of the pulsation.

A further stepwise growth in the ion signal to 5902 ± 251 counts/s was observed as the spray regime transitioned from axial mode II to mode III at 3800 V (see Figure 6B). In addition to the ion yield, in axial mode III the dc component of the total spray current grew to 109 ± 4 nA with no appreciable ac component present. This was accompanied by continuous ejection of charged droplets, also improving the duty cycle of analyte sampling by the electrospray source. Surprisingly, the survival yield of the thermometer ions increased as the spraying mode switched to cone-jet mode, indicating that slightly softer ion production took place in this regime. Compared to axial mode II, for the axial III regime $\sim 13\%$ higher survival yields were observed (see the top curve in Figure 6B).

There could be various explanations for the enhanced survival yield. First, as demonstrated before, the axial II spraying regime generates droplets of much larger size and stronger heterogeneity than axial III. As the droplets fly through the differential pumping region (kept at 1.7×10^2 Pa pressure) in the mass spectrometer, the solvent evaporates. The produced solvent load in this region is proportional to the third power of the droplet size. For example, if compared to the cone-jet mode an order of magnitude larger droplets were sampled in the pulsating Taylor cone regime, the amount of produced vapor would be 1000 times larger. This might, at least locally, increase the pressure of the background gas, result-

ing in more collisions and reduced survival yields. The gauge assigned to this region, however, showed no change in the pressure upon the spraying mode switch, probably because of the high pumping speeds used in the vacuum system. To address this question, the exhaust volume rate of the vacuum system could be measured and compared between the spraying regimes. This approach had detected vapor load differences between on-axis and off-axis electrospray source configurations.⁵⁵ Alternatively, the effect of evaporative droplet cooling^{56,57} has to be considered. For micrometer-sized droplets a recent investigation showed that decreasing background pressure resulted in decreased droplet temperatures and the evaporative cooling rate was inversely proportional to the droplet radius.⁵⁸ As the cone-jet mode yields much smaller droplets than axial II, the droplets produced in this regime can be expected to undergo faster cooling. The cooling effect is further enhanced because the background pressure drops by at least 3 orders of magnitude as the droplets move from atmospheric pressure toward the skimmer. Lower temperature droplets can produce ions with lower internal energy and higher survival yield.

Electrochemical Redox Reactions. We also explored whether the extent of electrochemical oxidation of reserpine was a function of the spraying regime. The degree of oxidation was characterized by the ratio of the reduced (m/z 609) and oxidized (m/z 607) molecular ion intensities. The other possible oxidation steps yielded relatively low (m/z 605) or stable (m/z 625) ion intensities (see Figure 6A); thus, only the first step was considered in the analysis. The actual pathway of oxidation in ESI is dependent on the experimental conditions. In one set of experiments a reserpine (m/z 609) oxidation pathway going through dehydrogenation (m/z 607) followed by hydroxylation (m/z 625) was identified (see Figure 3 in ref 59).⁵⁹ Later the oxidation of reserpine (m/z 609) was observed to go first through oxygen addition (m/z 625) followed by water loss (m/z 607) (see Scheme 1 in ref 60).⁶⁰ No matter which oxidation pathway the reaction follows, the effect of spraying modes on the degree of oxidation remains valid.

The detected protonated reserpine intensity, $I(\text{Res}^+)$, and the calculated $I(\text{Res}^+)/I(\text{Res} - 2\text{H})^+$ ratio are shown in Figure 6C as a function of the spray voltage. Increasing the emitter voltage in axial mode II resulted in a slow rise of the reserpine signal but no observable change in the extent of oxidation. As the spraying regime changed to cone-jet mode at 3800 V, approximately an order of magnitude higher reserpine ion intensities were recorded. The dramatic increase in ion yields coincided with a large reduction in droplet sizes to the submicrometer domain. These smaller droplets require fewer generations of fission to reach the nanodroplet size range (~ 10 nm) believed to be most efficient in ion production. The linear regression in Figure 6C also indicated that, compared to the pulsating Taylor cone regime, a 35% higher $I(\text{Res}^+)/I(\text{Res} - 2\text{H})^+$ ratio was present in cone-jet mode; i.e., there was significantly less analyte oxidation in this regime.

(55) Voyksner, R. D.; Lee, H. *Anal. Chem.* **1999**, *71*, 1441–1447.

(56) Fisenko, S. P.; Brin, A. A.; Petruichik, A. I. *Int. J. Heat Mass Transfer* **2004**, *47*, 165–177.

(57) Francois, M.; Shyy, W. *Prog. Aerospace Sci.* **2002**, *38*, 275–304.

(58) Fisenko, S. P.; Wang, W. N.; Lenggoro, I. W.; Okuyama, K. *Chem. Eng. Sci.* **2006**, *61*, 6029–6034.

(59) Van Berkel, G. J.; Asano, K. G.; Granger, M. C. *Anal. Chem.* **2004**, *76*, 1493–1499.

(60) Kertesz, V.; Berkel, G. J. V.; Granger, M. C. *Anal. Chem.* **2005**, *77*, 4366–4373.

(54) Wysocky, V. H.; Kenttamaa, H. I.; Cooks, R. G. *Int. J. Mass Spectrom. Ion Processes* **1987**, *75*, 181–208.

To qualitatively explain this observation, first let us consider the electrospray emitter as a cylinder-shaped electrochemical cell in which the stainless steel wall acts as an anode. Other parts of the ion source with lower potential (e.g., counter electrode or the inlet of the mass spectrometer) can serve as an auxiliary electrode. As the solution flows through the needle, electroactive components, such as reserpine, can be oxidized at the metal–liquid interface. Meanwhile the solution with excess positive charge is continuously removed by electrostatic spraying.

From the fluid dynamics perspective, two major regions of the emitter can be distinguished. The first region corresponds to the cylindrical volume within the needle. Here, for both capillaries used in our experiment the calculated Reynolds numbers (0.09 for the model 90525 Hamilton and 0.02 for the New Objective needle) predict laminar flow. Under these conditions the electrochemical oxidation occurs in the stagnant layer formed next to the capillary wall, while radial mass transport is responsible for carrying the oxidized species away from the surface and bringing electrochemically active components to it. Due to the fixed flow rate, the flow pattern in this region is independent of the spraying mode. The other region of importance for liquids of intermediate conductivity is the tip of the capillary in contact with the electrified meniscus. For the cone-jet regime, axisymmetric circulation exists within the cone. The tangential stress at the cone surface accelerates the fluid, whereas the flow is directed backward at the center.⁶¹ This results in a circulation in the steady Taylor cone that increases the residence time of the analyte in the tip region and somewhat enhances the probability of electrochemical oxidation. On the other hand, in pulsating Taylor cones the flow pattern is turbulent. This results in significantly enhanced mixing and more efficient transport of the analyte to the capillary surface. As a result, compared to axial mode III, there is enhanced oxidation of reserpine in axial mode II (see Figure 6C).

Another possible explanation can be based on viewing the electrospray source as a controlled-current electrolytic cell.⁶² In cone-jet mode a significantly higher spray current can be measured, indicating that more charge is being ejected per unit time. Since this charge removal must be balanced by the charge production at the liquid–metal interface to maintain neutrality, it follows that in axial mode III enhanced oxidation must occur. Under these conditions in a controlled current cell the electrochemical potential of the capillary shifts to higher values and other electroactive components might be oxidized. The oxidation of the most abundant component, water, leads to the acidification of the solution: $2\text{H}_2\text{O} \rightarrow 4\text{H}^+ + \text{O}_2 + 4\text{e}^-$, $E^\circ = +1.23 \text{ V}$.^{24,26} The appearance of competing reactions might explain why less analyte oxidation is observed in cone-jet mode. The electrochemical acidification also explains the more pronounced gain in the molecular ion yield of reserpine, a compound that requires protonation, compared to the thermometer ions that are present as preformed ions.

Finally, the combined effect of in-source dissociation and redox processes was demonstrated as a function of spraying regimes. An acidified (with 0.1% acetic acid) methanol solution (50%) of reserpine ($1 \times 10^{-5} \text{ M}$) was electrosprayed through a tapered tip (100 μm i.d.) metal needle at a 1.0 $\mu\text{L}/\text{min}$ flow rate. The mass

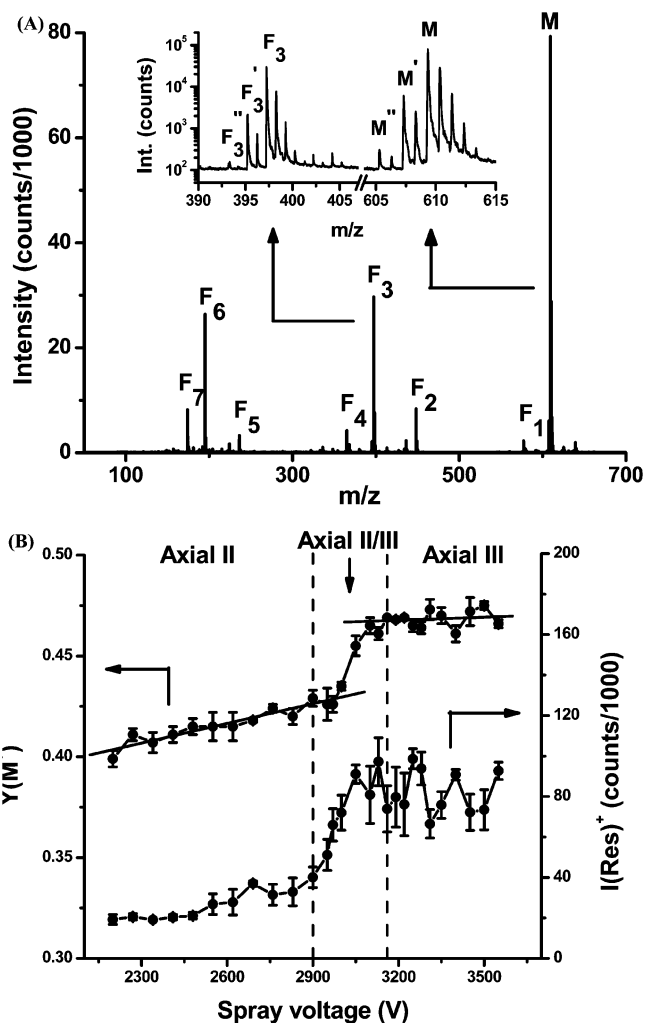


Figure 7. (A) Mass spectrum showing the combined effect of reserpine fragmentation and oxidation at the onset of the cone-jet regime (3160 V spray voltage). (B) Molecular ion yield (left axis) and molecular ion intensities (right axis) for reserpine. Symbols for fragments and oxidized species are listed in Table 1. Vertical dashed lines indicate boundary between electrospray modes. Equations for linear regression are $SY_{\text{axial II}} = 0.332 + (3.260 \times 10^{-5})U_{\text{spray}}$ and $SY_{\text{axial III}} = 0.452 + (4.970 \times 10^{-5})U_{\text{spray}}$.

spectrum in Figure 7A indicates that the analyte follows multiple channels of fragmentation; the most important dissociation pathways (F_1 through F_7) are listed in Table 1. Oxidation of the reserpine also took place, yielding $(M - 2\text{H} + \text{H})^+$ and $(F_3 - 2\text{H} + \text{H})^+$ ions with significant abundances, and $(M - 4\text{H} + \text{H})^+$ and $(F_3 - 4\text{H} + \text{H})^+$ ions were also detected (see the logarithmic intensity scale in the inset). Considering the seven dissociation and two oxidation pathways for reserpine, the yield of molecular ions was calculated as

$$Y(\text{M}^+) = \frac{I(\text{M}^+)}{I(\text{M}^+) + \left[\sum_{i=1}^7 I(\text{F}_i^+) \right] + [I(\text{M}^{2+}) + I(\text{F}_3^{2+})]} \quad (1)$$

The yield of intact reserpine ions and the corresponding ion intensity are depicted in Figure 7B as a function of the spray

(61) Hayati, I.; Bailey, A.; Tadros, T. F. *J. Colloid Interface Sci.* **1987**, *117*, 222–230.

(62) van Berkel, G. J.; Zhou, F. M. *Anal. Chem.* **1995**, *67*, 2916–2923.

Table 1. Dominant In-Source Fragmentation and Electrochemical Oxidation Products Observed for 3MO-BP and Reserpine

analyte	molecular ion	nominal m/z							oxidized species	
		fragment ion (s)								
3MO-BP	200 (T)	121 (F _T)							n/a	
reserpine	609 (M)	577 (F ₁)	448 (F ₂)	397 (F ₃)	365 (F ₄)	236 (F ₅)	195 (F ₆)	174 (F ₇)	607 (M')	395 (F ₃)

voltage. The figure shows trends, for the ion intensities and for the yields of the protonated analyte, similar to those seen for the fragmentation of the 3MO-BP thermometer ion and the oxidation of reserpine. First increasing the needle potential results in a slow enhancement in both the measured abundance and the calculated $Y(M^+)$. Then, as the regime change occurs, a sudden increase can be seen in both values with approximately 4 times higher ion intensities and 10% higher molecular ion yields for reserpine.

These results demonstrate the benefits of the cone-jet regime (e.g., enhanced ion production) over other axial spraying modes for analytical application of ESI. These data along with the example of the 3MO-BP thermometer ion also show that the extent of fragmentation can be shifted to a certain degree by adjusting the spraying mode. For the study of fragile compounds a cone-jet regime can be established, whereas the in-source fragmentation of an ion can be enhanced by maintaining a pulsating Taylor cone regime.

CONCLUSIONS

Electrospray ionization sources remain at the forefront of ion production in biomedical mass spectrometry. Other applications of the electrospray process include its emerging use for droplet production and delivery in spotting devices, in MALDI sample preparation, and most recently as a nebulizer for inductively coupled plasma mass spectrometry. All of these applications can benefit from a better understanding of the complex interplay among spraying conditions, electrohydrodynamics at the liquid meniscus, droplet fission in the spray plume, and ion production.

With the increased utility of these applications, fundamental studies are encouraged and a more complex view of the ES process is emerging. The electrohydrodynamic stability of the spray had been linked to the firm anchoring of the contact line between the liquid meniscus and the capillary. Empirical studies offered two practical solutions to the stability issues. First, tapered tip capillaries were introduced. Compared to the blunt tip design, they exhibited a broader stability region due to the firm anchoring of the liquid at the edgelike orifice. A second, more recent attempt to provide a better meniscus definition is the hydrophobic modification of the capillary tip.

Ion production yields seem to be strongly influenced by the size of the generated droplets. Nanosprays are known to produce submicrometer droplets and, correspondingly, higher ion yields. Experiments with narrow capillaries also showed that in these devices the liquid meniscus and probably the produced droplets carry more charge. The present study also demonstrated that operating the spray in cone-jet mode not only produces smaller droplets but also results in significantly higher ion yields.

In addition to the altered yields, we found that the chemical nature of the produced ions also correlated with the spraying

modes. A mild variation of the internal energy, and thus the fragmentation of the produced ions, was linked to spraying mode changes. Due to electrochemical effects, the pH, acid–base chemistry, and redox processes also showed a dependence on the spraying mode.

Our studies indicated that the factors responsible for the mode change effects were manifested through the variations in meniscus dynamics, the resulting droplet size distribution changes, the ensuing differences in the radial segregation of droplets, the significant variations in the duty cycle, and the changes in the dc and ac components of the spray current. Although changes in droplet sizes, and to some extent plume chemistry, as a function of spraying conditions (voltage and liquid flow rate) had been known in the literature, here we illustrated that the most substantial variations were not associated with simple spraying voltage changes but with the appearance of different spraying modes. Due to the hysteresis in these processes, we were able to establish two different spraying modes at the same voltage. The results clearly indicated that the spraying regime had the primary effect.

The results presented in this work promise potential improvements achievable in the analytical performance of ESI-MS by the active control of the spraying mode. This can be achieved by either optically analyzing the structure of the spray (as implemented in a recent report³⁸) or by following the temporal behavior of the spray current. However, changes in the directionality of the spray plume cannot be detected using a single counter electrode. For example, in an ESI source significant signal intensity loss might result from a change between axial and nonaxial regimes. These modes are undistinguishable by total spray current measurement on a single electrode. A solution could be based either on the combination of optical (similar to the imaging described in this work) and spray current measurements or on the use of a multisegmented counter electrode. For example, using a combination of four concentric ring sections of a metal plate with an orifice in the middle, one would be able to monitor the current captured on each electrode segment and ultimately derive a radial current distribution. This could serve as a simple device to monitor the deflection of the spray in an automated system for the active control of the spraying regime.

ACKNOWLEDGMENT

This material is based upon work supported by the National Science Foundation under Grant No. 0415521 and by the Research Enhancement Funds of the George Washington University. Any opinions, findings, and conclusions or recommendations expressed in this material are those of the author(s) and do not necessarily reflect the views of the National Science Foundation.

SUPPORTING INFORMATION AVAILABLE

Three fast imaging sequences with 10 μs delay increments were assembled into movies depicting the liquid ejection. The file names and experimental conditions are as follows. File *Axial I liquid ejection in the middle of burst.gif* shows a Hamilton 50525 needle (o.d./i.d. = 510/260 μm) spraying 50% methanol at a 2 $\mu\text{L}/\text{min}$ flow rate and 3400 V voltage in burst mode. The ejection corresponds to the highest intensity current peak within the burst. File *Axial II liquid ejection large ID needle.gif* shows a Hamilton 50525 needle (o.d./i.d. = 510/260 μm) spraying 50% methanol at 5 $\mu\text{L}/\text{min}$ flow rate and 2800 V voltage. The ejection cycle

repeats itself with a well-defined period. File *Axial II liquid ejection small ID needle.gif* shows a Hamilton 90531 needle (i.d./o.d. = 260/130 μm) spraying 50% methanol acidified with 0.1% (v/v) acetic acid at a 2 $\mu\text{L}/\text{min}$ flow rate and 3400 V voltage. This material is available free of charge via the Internet at <http://pubs.acs.org>.

Received for review December 17, 2006. Accepted January 25, 2007.

AC062382I